

## Chapter 6

# Frame localisation optical projection tomography

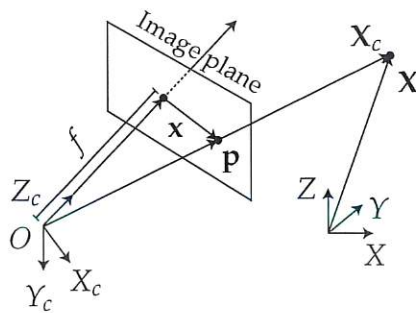
In the previous chapters, volumetric imaging was achieved using wide-field imaging and a relative scanning motion between the system's focal plane and the sample. Volumetric imaging can also be achieved by rotating a sample and tomographically reconstructing the 3D distribution of a signal (scattering, absorption of luminosity) within the specimen. Accurate tomographic reconstruction relies heavily on precision movement and rotation. Here an algorithm will be presented that relies exclusively on multiple (5+) tracked fiducial beads to enable accurate reconstruction even with systematic mechanical drift. It will be used on ground truth simulated testcard image data with motion errors compounded onto the tomographic rotation. These errors will include systematic mechanical drift, giving a spiral path; and angular drift giving precession.

The projective mathematics introduced in Chapter 5 is a ~~small~~ part of a field of mathematics used in computer vision to localise (in 3D) points in space as projected onto multiple view points. The algorithm presented in this chapter will use an extension of this projective mathematics to reconstruct OPT volumes from the set of rotational projections. Considerations were made to combine OPT and light-sheet imaging within the system constructed in Chapter 4, though this was never realised during this thesis.

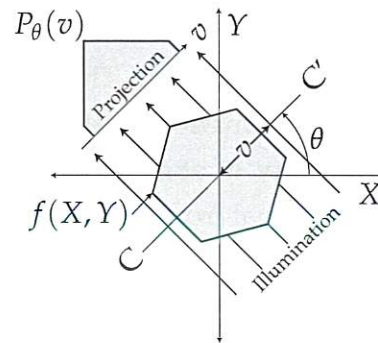
*It should be noted that, due to conventions within the field of computer vision, all lab frame or world coordinates will be represented as capital letters (ex.  $X$ ,  $X_c$ ) and image frame*

If software is on github,  
say so here.

*coordinates will be represented in image plane coordinates (ex.  $\mathbf{x}$ ) in this chapter, shown in Fig. 6.1a.*



(a) Coordinate system used in this chapter describing a camera with an associated image plane one focal distance  $f$  away, imaging an object at point  $X$ .



(b) From an angle  $\theta$ , an object  $f(X, Y)$  and its projection  $P_\theta(t)$  are known.

**Fig. 6.1**  $X_c = (X_c, Y_c, Z_c)$  is the camera-centered coordinate point in 3D space.  $X = (X, Y, Z)$  is the world coordinate point in 3D space.  $p = (x, y, f)$  is the ray vector to point of image plane.  $x = (x, y)$  is the image plane coordinates.  $w = (u, v)$  is the pixel coordinates (not shown) corresponding to the point  $x$  (not shown). The optical axis travels along the  $Z_c$  axis through the image plane.

## 6.1 Rotational computer tomography in microscopy

Sharpe *et.al* proposed OPT in 2002 [63] using visible light to image transparent or translucent mesoscopic samples, with micrometer resolution. OPT addresses a scale gap between ~~the~~ photographic techniques (samples larger than 10 mm), and light microscopy techniques (samples smaller than 1 mm) to image biological samples in the 1 mm to 10 mm regime. OPT is based on computerised tomography techniques [[17]] in which a set of projections of a specimen are imaged as the specimen travels through a full rotation. Algorithms exist to then transform this set of images into a 3D image stack in Cartesian  $(X, Y, Z)$  coordinates. OPT is non-invasive optically but may require specialist invasive preparation for its samples. There are two imaging modalities for OPT, emission Optical Projection Tomography (eOPT) and transmission Optical Projection Tomography (tOPT). In eOPT, a fluorescent sample is excited using an illumination source off axis to the detection, similar to light-sheet but the entire depth of field of the detection of objective is illuminated. Scattered illumination photons are rejected at the detector using an appropriate filter. In tOPT, a white-light source with a diffuser and a collimator is placed along the optical axis to provide near-collimated, uniform illumination onto the sample for transmission to a detector opposite (see Fig. 6.1b). Each photosite at

Be prepared to explain, in vivo, that  $p$  and  $X_c$  are not necessarily colinear, but are related by linear transforms. (I think).

typically



the detector corresponds to a ray that has passed through the sample and been attenuated by the sample. The eOPT and tOPT modes can work in unison to provide contextual information, with the transmission images indicating overall structure (optical density of absorption or scattering) which can be supplemented by the fluorescent signal from a label of interest.

### 6.1.1 Reconstruction

As the sample is rotated each pixel collects an intensity  $I(\theta) = I_n e^{-k}$  at discrete ( $n$ ) angles through a full rotation of the sample; where  $I_n$  is the unattenuated radiation intensity from the source to the detector,  $k$  is the attenuation caused by the sample along a detected ray and  $I(n)$  is the measured intensity, see Fig. 6.1b. Rays from the sample to the detector approximate straight lines, and so the rays reaching the detector with a line integrals. A projection is then the resulting intensity profile at the detector for a rotation angle, and the integral transform that results in  $P_\theta(v)$  is the Radon transform.

The equation of a set of parallel rays from a source passing through the specimen to a point  $v$  along the detector is:

$$X \cos(\theta) + Y \sin(\theta) - v = 0 \quad (6.1)$$

Projecting many such rays through a sample with structure  $f(X, Y)$  gives:

$$P_\theta(v) = \int_{-\infty}^{\infty} \int_{-\infty}^{\infty} f(X, Y) \delta(x \cos(\theta) + y \sin(\theta) - v) dX dY \quad (6.2)$$

Where  $P_\theta(v)$  is the Radon transform of  $f(X, Y)$  which represents the contrast image of 2D slice of the specimen. The Radon transform of an image produces a sinogram as in Fig. 6.2

An inverse Radon transform is used to recover the original object from the projection data; which is achieved by taking the Fourier transform of each projection measurement, then reordering the information from the sample into the respective position in Fourier space. This is valid due to the Fourier Slice theorem (see Appendix ?? for a derivation) [64], which states that the Fourier transform of a

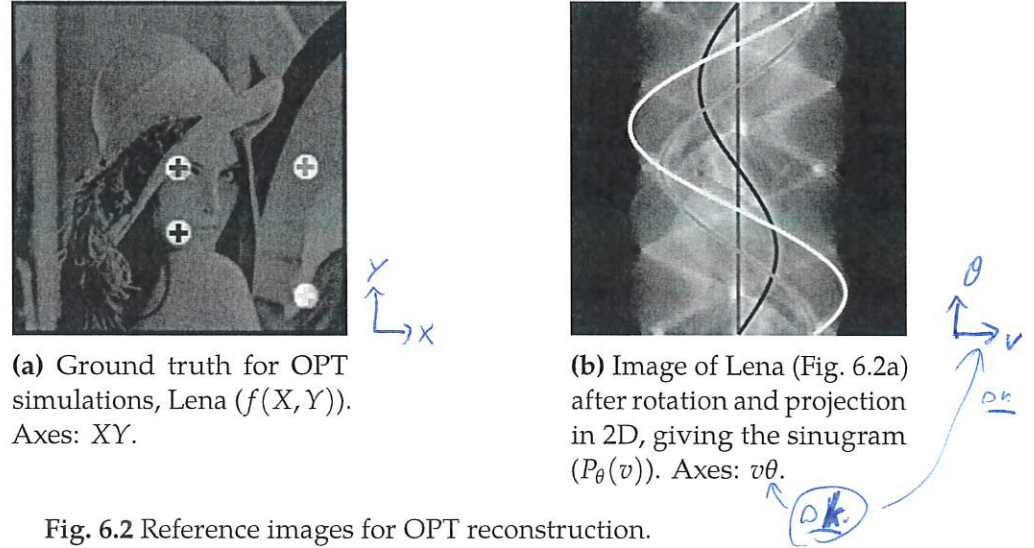


Fig. 6.2 Reference images for OPT reconstruction.

parallel projection is equivalent to a 2D slice of the Fourier transform original sample.

$$f_{\text{fb}}(X, Y) = \int_0^\pi Q_\theta(X \cos(\theta) + Y \sin(\theta), \theta) dX dY \quad (6.3)$$

Where  $Q_\theta$  is the filtered projection data, and  $f_{\text{fb}}(X, Y)$  is the back-projected image. A spatial filtering step is applied during back-projection to avoid spatial frequency oversampling during the object's rotation (see Fig. 6.5b) a high pass filter is commonly used to compensate for the perceived blurring. The blurring arises as  $Q_\theta$  is back-projected (smeared) across the image plane for each angle of reconstruction; which means that not only does the back-projection contribute at the line it is intended to (along line C in Fig. 6.1a), but all other points along the back-projecting ray.

## Aim

The Radon transform relies heavily on the assumption of circular motion with constant angular steps about a vertical axis. This chapter presents an improved reconstruction method which explains, some of the techniques used in stereoscopic imaging to register back projections rather than relying on line integrals. The algorithm proposed here is therefore robust to mechanical drifts across acquisitions as well as inconsistent angular steps

## 6.2 Stereoscopic imaging

Imaging scenes in stereo allows for the triangulation of individual features in three dimensional space (known as world points) when the features or fiducial markers in one detector are uniquely identifiable (such as fluorescent beads).

Triangulation requires each feature to be detected in both images of a stereo imaging system, and for these detections to be correctly associated with one another: this is known as the correspondence problem. Many methods exist to ensure that features are detected from image data and accurately associated between two cameras or views. Properties of scale independent features and their surrounding pixel environment in one image can be matched to a similar feature in the second image.

Now, suppose we know the relative positions of the two cameras and their respective intrinsic parameters, such as magnification and pixel offset. For a single camera and given the camera parameters, we can translate pixel coordinates,  $\mathbf{w} = (u, v)$ , into the coplanar image plane coordinates  $\mathbf{x} = (x, y)$ :

$$u = u_0 + k_u x \quad (6.4)$$

$$v = v_0 + k_v y \quad (6.5)$$

Knowing the focal length ( $f$ ) of the imaging system, image plane coordinates may be projected into a ray in 3D. The ray can be defined by using the point  $\mathbf{p}$  in camera-centred coordinates, where it crosses the image plane.

$$\mathbf{p} = \begin{bmatrix} x \\ y \\ z \end{bmatrix} \quad (6.6)$$

From the definition of a world point, as observed through an image, we can construct a dual-view model of world points in space as in Fig. 6.3. Using a model of a system with two views allows for the triangulation of rays based on image correspondences, this is an important part of stereo-vision. The most important matching constraint which can be used is the *epipolar constraint*, and follows directly from the fact that the rays must intersect in 3D space. Epipolar constraints facilitate

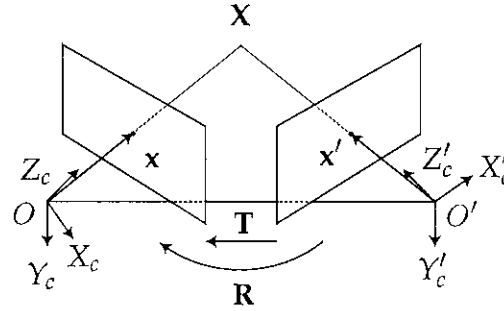


**Fig. 6.3** Epi-polar geometry described for two adjacent views (or cameras of a scene). Coordinates as expressed in Fig. 6.1a with prime notation (') denoting the additional right camera view. Transforming from right to left camera-centered coordinates ( $X'_c$  to  $X_c$ ) requires a rotation ( $R$ ) and a translation ( $T$ ).

the search for correspondences, they constrain the search to a 1D line in each image. To derive general epipolar constraints, one should consider the epipolar geometry of two cameras as seen in Fig. 6.3

The **baseline** is defined as the line joining the optical centres. An **epipole** is the point of intersection of the baseline with the image plane and there are two epipoles per feature, one for each camera. An **epipolar line** is a line of intersection of the epipolar plane with an image plane. It is the image in one camera of the ray from the other camera's optical centre to the world point ( $X$ ). For different world points, the epipolar plane rotates about the baseline. All epipolar lines intersect the epipole.

The epipolar line constrains the search for correspondence from a region to a line. If a point feature is observed at  $x$  in one image frame, then its location  $x'$  in the other image frame must lie on the epipolar line. We can derive an expression for the epipolar line. The two camera-centered coordinate systems  $X'_c$  and  $X_c$  are related by a rotation,  $R$  and translation,  $T$  (see in Fig. 6.3) as follows:

$$X'_c = RX'_c + T \quad (6.7)$$

Taking the vector product with  $T$ , we obtain

$$T \times X'_c = T \times RX'_c + T \times T \quad (6.8)$$

$$T \times X'_c = T \times RX'_c \quad (6.9)$$

### 6.2.1 The Essential matrix

Taking the scalar product with  $\mathbf{X}'_c$  of (6.9), we obtain:

$$\mathbf{X}'_c \cdot (\mathbf{T} \times \mathbf{X}_c) = \mathbf{X}'_c \cdot (\mathbf{T} \times \mathbf{R}\mathbf{X}'_c) \quad (6.10)$$

$$\mathbf{X}'_c \cdot (\mathbf{T} \times \mathbf{R}\mathbf{X}_c) = 0 \quad (6.11)$$

A vector product can be expressed as a matrix multiplication:

$$\mathbf{T} \times \mathbf{X}_c = \mathbf{T}_\times \mathbf{X}_c \quad (6.12)$$

where

$$\mathbf{T}_\times = \begin{bmatrix} 0 & -T_z & T_y \\ T_z & 0 & -T_x \\ -T_y & T_x & 0 \end{bmatrix} \quad (6.13)$$

So equation (6.9) can be rewritten as:

$$\mathbf{X}'_c \cdot (\mathbf{T}_\times \mathbf{R}\mathbf{X}_c) = 0 \quad (6.14)$$

$$\mathbf{X}'_c \mathbf{T} \mathbf{E} \mathbf{X}_c = 0 \quad (6.15)$$

where

$$\mathbf{E} = \mathbf{T}_\times \mathbf{R} \quad (6.16)$$

$\mathbf{E}$  is a  $3 \times 3$  matrix known as the *essential matrix*. The constraint also holds for rays  $\mathbf{p}$ , which are parallel to the camera-centered position vectors  $\mathbf{X}_c$ :

$$\mathbf{p}'^T \mathbf{E} \mathbf{p} = 0 \quad (6.17)$$

This is the epipolar constraint. If a point  $\mathbf{p}$  is observed in one image, then its position  $\mathbf{p}'$  in the other image must lie on the line defined by Equation (6.17). The essential matrix can convert from pixels on the detector to rays  $\mathbf{p}$  in the world, assuming a calibrated camera (intrinsic properties are known), and pixel coordinates can then

Seems.  
Ok, - have  
not checked  
much...



be converted to image plane coordinates using:

$$\begin{bmatrix} u \\ v \\ 1 \end{bmatrix} = \begin{bmatrix} k_u & 0 & u_0 \\ 0 & k_v & v_0 \\ 0 & 0 & 1 \end{bmatrix} \begin{bmatrix} x \\ y \\ 1 \end{bmatrix} \quad (6.18)$$

We can modify this to derive a relationship between pixel coordinates and rays:

$$\begin{bmatrix} u \\ v \\ 1 \end{bmatrix} = \begin{bmatrix} \frac{k_u}{f} & 0 & \frac{u_0}{f} \\ 0 & \frac{k_v}{f} & \frac{v_0}{f} \\ 0 & 0 & \frac{1}{f} \end{bmatrix} \begin{bmatrix} x \\ y \\ f \end{bmatrix} \quad (6.19)$$

$\tilde{\mathbf{K}}$  is defined as follows:

$$\tilde{\mathbf{K}} = \begin{bmatrix} fk_u & 0 & u_0 \\ 0 & fk_v & v_0 \\ 0 & 0 & 1 \end{bmatrix} \quad (6.20)$$

then we can write pixel coordinates in homogenous coordinates:

$$\tilde{\mathbf{w}} = \tilde{\mathbf{K}}\mathbf{p} \quad (6.21)$$

### 6.2.2 The Fundamental matrix

From (6.17) the epipolar constraint becomes

$$\tilde{\mathbf{w}}'^T \tilde{\mathbf{K}}^{-T} \mathbf{E} \tilde{\mathbf{K}}^{-1} \tilde{\mathbf{w}} = 0 \quad (6.22)$$

$$\tilde{\mathbf{w}}'^T \mathbf{F} \tilde{\mathbf{w}} = 0 \quad (6.23)$$

The  $(3 \times 3)$  matrix  $\mathbf{F}$ , is called the *fundamental matrix*. With intrinsically calibrated cameras, structure can be recovered by triangulation. First, the two projection matrices are obtained via a Singular Value Decomposition (SVD) of the essential matrix. The SVD of the essential matrix is given by:

$$\mathbf{E} = \mathbf{K}'^T \mathbf{F} \mathbf{K} = \mathbf{T}_\times \mathbf{R} = \mathbf{U} \mathbf{\Lambda} \mathbf{V}^T \quad (6.24)$$

It can be shown that

$$\hat{\mathbf{T}}_\times = \mathbf{U} \begin{bmatrix} 0 & 1 & 0 \\ -1 & 0 & 0 \\ 0 & 0 & 0 \end{bmatrix} \mathbf{U}^T \quad (6.25)$$

and

$$\mathbf{R} = \mathbf{U} \begin{bmatrix} 0 & -1 & 0 \\ 1 & 0 & 0 \\ 0 & 0 & 1 \end{bmatrix} \mathbf{V}^T \quad (6.26)$$

Then, aligning the left camera and world coordinate systems gives the projection matrices:

$$\mathbf{P} = \mathbf{K} \begin{bmatrix} \mathbf{I} & | & \mathbf{0} \end{bmatrix} \quad (6.27)$$

and

$$\mathbf{P}' = \mathbf{K}' \begin{bmatrix} \mathbf{R} & | & \mathbf{T} \end{bmatrix} \quad (6.28)$$

Where  $\begin{bmatrix} \mathbf{I} & | & \mathbf{0} \end{bmatrix}$  is the identity matrix augmented column-wise with a zero matrix, and the two projection matrices ( $\mathbf{P}$  and  $\mathbf{P}'$ ) project from camera pixel coordinates to world coordinates. Given these projection matrices, scene structure can be recovered (only up to scale, since only magnitude of  $\mathbf{T}$  ( $|\mathbf{T}|$ ) is unknown) using least squares fitting. Ambiguities in  $\mathbf{T}$  and  $\mathbf{R}$  are resolved by ensuring that visible points lie in front of the two cameras. As with the essential matrix, the fundamental matrix can be factorised into a skew-symmetric matrix corresponding to translation and a  $3 \times 3$  non-singular matrix corresponding to rotation.

## 6.3 The proposed algorithm

The shift of a camera or a camera pair around a scene separated by a transformation matrix ( $\begin{bmatrix} \mathbf{R} & \mathbf{T} \end{bmatrix}$ ) is analogous to transforming the sample in the fixed view of an imaging detector, as in OPT. During a typical OPT acquisition, a marker will appear to follow an elliptical path in the  $XY$  plane. In the following volume reconstruction there will then be a fitting step to recover the path of the fiducial, to then apply a correction before applying a Radon transform. This type of reconstruction not only ignores any mechanical jitter of the sample but also any affine, systematic, mechanical drift ( $X, Y, Z, \theta, \phi, \psi$ ).

We have seen that using two adjacent images, of a scene separated by some rotation and translation, world points in 3D space may be triangulated within the scene given the rotational and translational matrices of the respect camera views. The inverse is also possible, given a sufficient number of known fiducial points in a scene the translation and rotation matrices can be recovered. The recovery of a more exact description of the motion of the scene can eliminate any need for a fitting and may recover and correct for drift, as well as eliminate any mechanical jitter. Errors may however then be introduced from fiducial markers mechanically slipping and localisation errors. Fiducial markers in this sense refer to an accurately locatable marker common through different views in a sample.

Once a sufficient amount of fiducial markers are reliably tracked from the first to the second image, the fundamental, essential and Homography matrices can be computed. Using the factorisation one of these matrixes, between each adjacent view of a rotating scene, the translation and rotational matrices may be recovered. Here we will discuss a reconstruction using  $\mathbf{F}$  but the same principle applies for  $\mathbf{E}$  and  $\mathbf{H}$ .

Here are two ways of reconstructing using the fundamental matrix as described above. The first method involves computing  $\mathbf{F}$  for two neighbouring images with 5 or more fiducial markers, having additional beads helps to remove ambiguity and increase confidence in  $\mathbf{F}$ . Once  $\mathbf{F}$  is calculated  $\mathbf{F}$  is then decomposed into  $\mathbf{R}_n$  and  $\mathbf{T}_n$  between each view  $n$  and  $n + 1$ . The image at view  $n + 1$  is then back projected along the virtual optical axis within a virtual volume where the sample will be reconstructed. The size of this back projection and virtual volume is chosen to be suitably large (so that important data is not lost). Then, all the prior rotation and translation matrices are serially multiplied from  $\begin{bmatrix} \mathbf{R}_0 & \mathbf{T}_0 \end{bmatrix}$  until  $\begin{bmatrix} \mathbf{R}_n & \mathbf{T}_n \end{bmatrix}$ , this final matrix is inverted and applied to the back projected volume. The matrix inversion

check:  
XY or XZ  
camera?

marker

is in  $XY$  plane

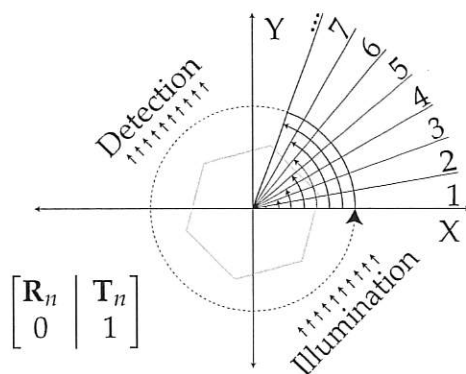


**Fig. 6.4** Principles of the proposed algorithm. Each successive frame of OPT image data will have an associated  $\mathbf{R}$  and  $\mathbf{T}$  (shown here in augmented form using homogenous coordinates), these matrices can be recovered from comparing each frame ( $n$ ) to its successor ( $n + 1$ ).



(a) This is the unfiltered reconstruction of the object using the Radon transform



(b) Ram-lak (Fourier ramp) filter applied to Fig. 6.5a.

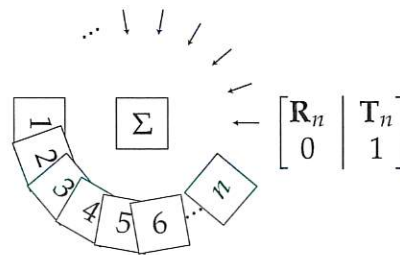
**Fig. 6.5** The result of a tomographic reconstruction (using equally spaced angular steps and no translation between frames) requires Fourier filtering to normalise spatial contrast.

step is important as it realigns the back projection in the volume to where it originally was compared respective of the first projection. This process is repeated for every angle and the back projected volume from each step is summed with every other step. Finally the remaining volume is filtered using a high-pass filter; here a Ram-Lak filter is used <sup>1</sup>. By producing a series of transformation matrices from adjacent acquisitions, errors compound and the reconstruction of volumes degrades with more projections, see Fig. 6.5.

The second approach is less prone to compound errors but relies on precise identification and tracking of fiducial markers. Instead of calculating  $\mathbf{F}$  between

<sup>1</sup>Linear real (amplitude) ramp filter in Fourier space





(a) Forward model

**Fig. 6.6** This figure illustrates the simulation of OPT data incorporating rotational and translational offsets, and the proposed reconstruction algorithm. (a): The  $n$  projections of the object ( $\Sigma$ ), at rotation ( $\mathbf{R}_n$ ) and translation ( $\mathbf{T}_n$ ), produces  $n$  frames of image data. (b): In the reconstruction algorithm, the rotational and translational matrices are recovered ( $\mathbf{R}'_n$  and  $\mathbf{T}'_n$ ) from triangulation of the fiducial markers. These transformation matrices are then used to obtain a contribution to the volumetric reconstruction from each observed frame and the summated reconstruction is assembled from the  $n$  frames. The now realigned back projections are summed to produce an unfiltered back projection. The transformation matrices are shown in augmented form using homogenous coordinates. During the OPT measurement,  $n$  projections of the object sigma are observed with rotations  $\mathbf{R}_1$  to  $\mathbf{R}_n$  and corresponding translations  $\mathbf{T}_1$  to  $\mathbf{T}_n$  where the translations account for imperfect alignment.

neighbouring images  $\mathbf{F}$  is calculated between the current projection and the very first projection.  $\mathbf{F}$  is then decomposed and the transformation matrix is inverted and applied to the back projected volume. The reoriented back projected volumes are summed and finally filtered to remove the additional spatial frequencies imparted from rotating the sample.

The second approach is robust against compound errors but an additional programatic step is needed to know which beads in the first image correspond to beads in the  $n^{\text{th}}$  image. This can be achieved using tracking and momentum particle tracking algorithms, though confounding issues can arise i.e. if a particle orbits too far away or occlusions occur. In both cases a decomposed  $\mathbf{F}$  matrix will produce four possible transformation pairs ( $\mathbf{R}, \mathbf{T}$ ;  $\mathbf{R}, -\mathbf{T}$ ;  $-\mathbf{R}, \mathbf{T}$ ;  $-\mathbf{R}, -\mathbf{T}$ ). Once the transformation matrix between the first view and the second view is calculated the proceeding transformation matrices are then easily chosen by similarity and general direction of motion. An example of this type of selection would be:

$$\min_{I(n)} \left[ I(n) = \left( \begin{bmatrix} \mathbf{R}_n & | & \mathbf{T}_n \end{bmatrix} - \begin{bmatrix} \mathbf{R}_{n-1} & | & \mathbf{T}_{n-1} \end{bmatrix} \right)^2 \right] \quad (6.29)$$

If you've removed Fig (b), edit caption.

$(\mathbf{R}_1 \text{ to } \mathbf{R}_n)$

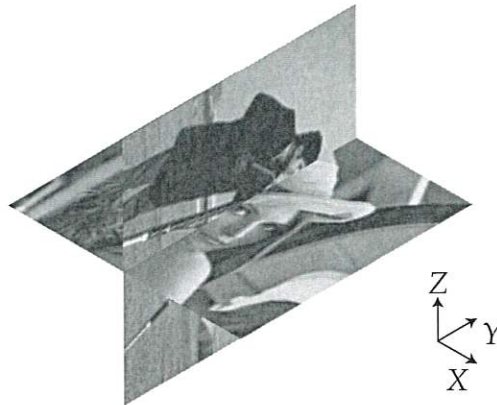
$(\mathbf{R}_1 \text{ to } \mathbf{R}_n)$  and  $(\mathbf{T}_1 \text{ to } \mathbf{T}_n)$

BECAUSE  $n=180$  is just one frame.

$\mathbf{R}_1 \text{ to } \mathbf{R}_n$   
and  
 $\mathbf{T}_1 \text{ to } \mathbf{T}_n$

from the  
first  
imaging  
plane





(a) Ground truth 3D object for reconstruction, based on the Cameraman and Lena testcard images. ✓

The first two views are more difficult to choose the correct decomposition for, but it is possible if a suitable ideal matrix is given as a comparison. Such an ideal matrix is composed using *a priori* knowledge of the likely angle of rotation of the system's imaging properties.

## 6.4 Verification of the proposed algorithm

To verify that the proposed algorithm successfully reconstructs the specimen, it was applied to simulated data. The image of Lena <sup>2</sup> is used here as a test image to verify the validity of each reconstruction. Superimposed on Lena are fiducial beads to track the rotation of the image, see Fig. 6.2a. The reference image was then rotated through 128 angles over  $2\pi$  radians and projected along the  $Y$  axis and a slice in  $(X, Y)$  was taken to create a single line projection, shown three dimensionally in Fig. 6.7. This is repeated for each angle with each line projection stacked to create a sinogram, see Fig. 6.2b.

In the standard approach for OPT reconstruction, the sinogram undergoes the inverse Radon transform, see Fig. 6.5a and then post-filtering, (see Fig. 6.5b. *as shown in*) This step is substituted for the proposed algorithm; in Fig. 6.9 the two techniques are compared for ideal conditions of smooth, predictable rotation. The proposed algorithm produces a faithful reconstruction on the original image, as shown in Fig. 6.8 Both techniques lose some of the original contrast of the object due to under-sampling of rotations. When taking the histogram of the absolute pixel-wise

<sup>2</sup>Standard reference image data

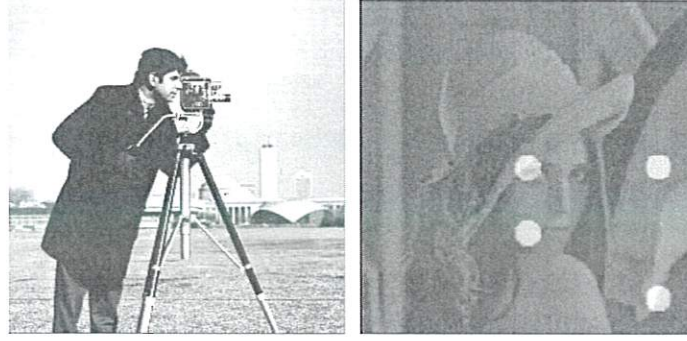


Fig. 6.8 Filtered reconstruction of the ground truth reference image from Fig. 6.7 using the new proposed algorithm. Axes:  $(X, Y)$

*↖ (x, z) for left hand image and (x, y) for right.*

difference between the original source image to the images produced by the new algorithm and the Radon transform, see Fig. 6.10. The mean square errors ( $MSE$ , see Equation (6.30)) of the new algorithm and the Radon transform are 15.01 % and 14.84 % respectively, see Fig. 6.10 for a histogram of a pixel-wise comparison. This suggests that the new algorithm is producing an accurate reconstruction of the object, similar to the standard Radon transform.

$$MSE = \frac{1}{n} \sum_{i=1}^n (Y_i - \hat{Y}_i)^2 \quad (6.30)$$

The more challenging case of a sample drifting, with a constant velocity, systematically along the  $X$  axis was then considered; this produced a helical path of a single fiducial within the sample, see Fig. 6.11b. In Fig. 6.12a, the Radon transform entirely fails to produce a recognisable reproduction of the test image with the addition of a slight helicity to the rotation. The proposed algorithm produces an equivalent result to that of a sample rotating without any systematic drift, see Fig. 6.5b. In Fig. 6.13 the respective images from each algorithm were compared, as before, while the helical shift was incremented. See Fig. 6.11b for a sinogram of a sample whereby a helical shift has been induced. When using correlation as a metric of reproduction quality, at zero helicity, the new algorithm fairs slightly worse at 94 % correlation compared to the Radon transform at 96 %. As expected, the Radon transform rapidly deteriorates once a systematic drift is applied; where-as the new algorithm maintains quality of reconstruction, see Fig. 6.13.

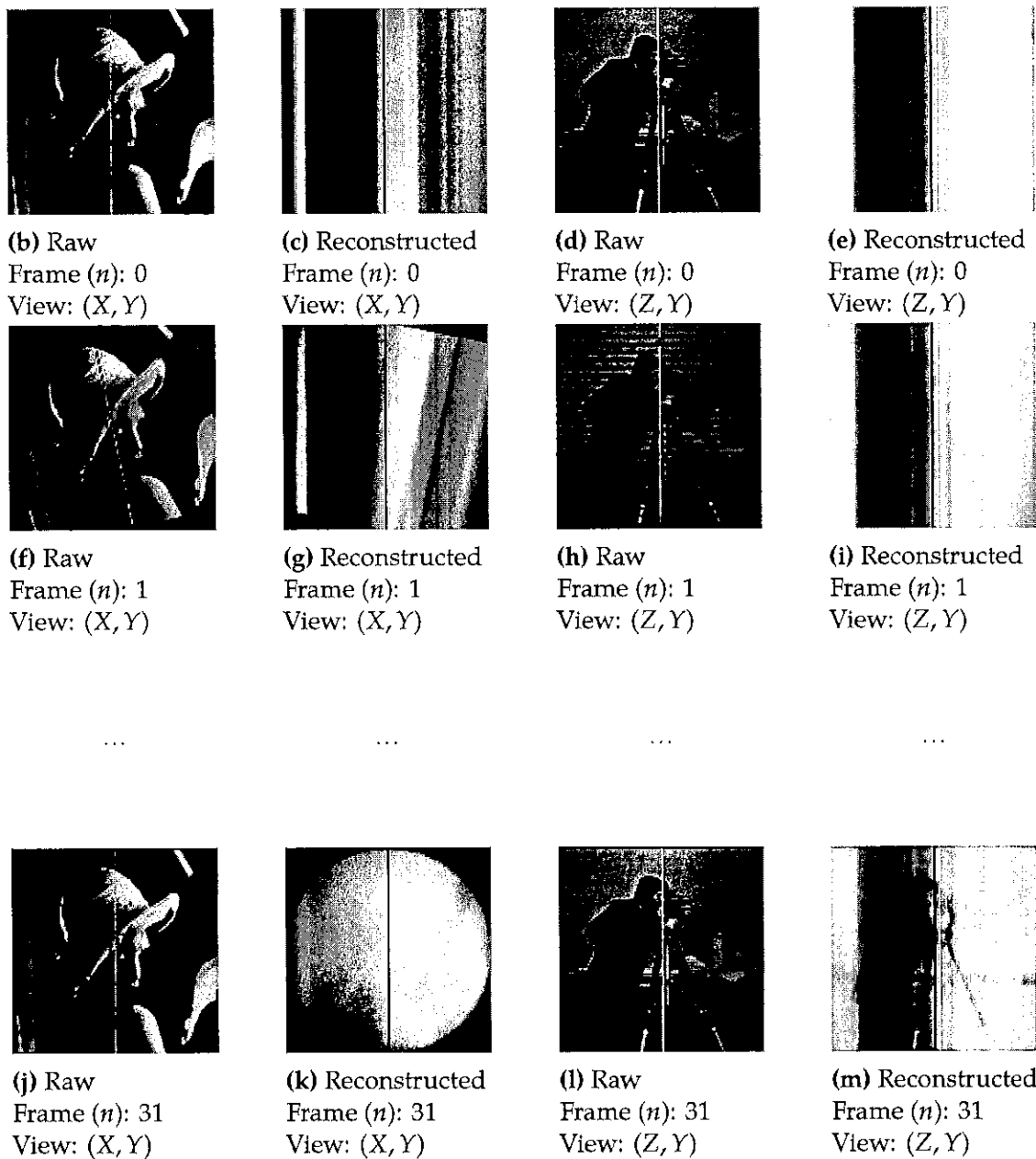


**Fig. 6.7** a 3D test-volume of two orthogonal and different testcard images was used to verify the reconstructive capabilities of the proposed algorithm. The projected image data (b), (h), (j) and (d), (h), (l), were used to iteratively generate reconstructions where the  $n$ th reconstruction incorporates all the information from observation 0 to  $n$ . The results are unfiltered for clarity of demonstrating the iterative reconstruction, which is applied in Fig. 6.8.

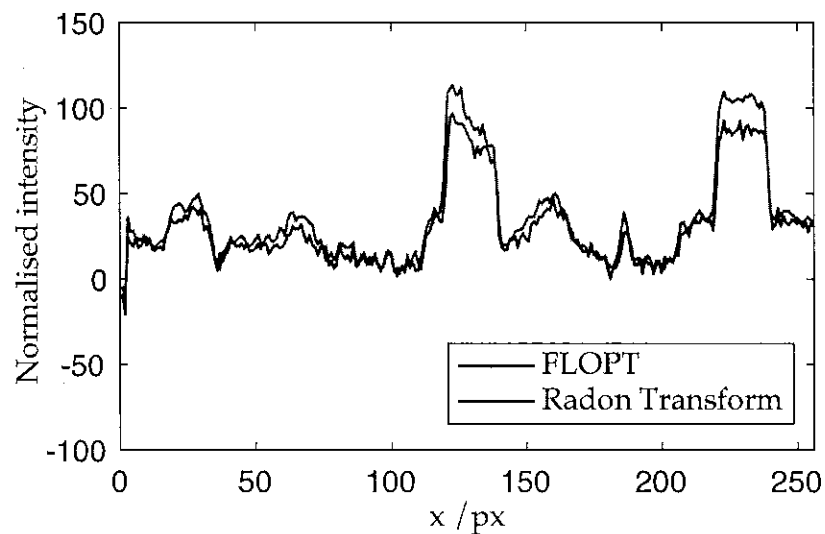


**Fig. 6.9** Line profile comparison of the reconstruction of a reference image computationally rotated, projected and reconstructed using the standard Radon transform and the new proposed algorithm.

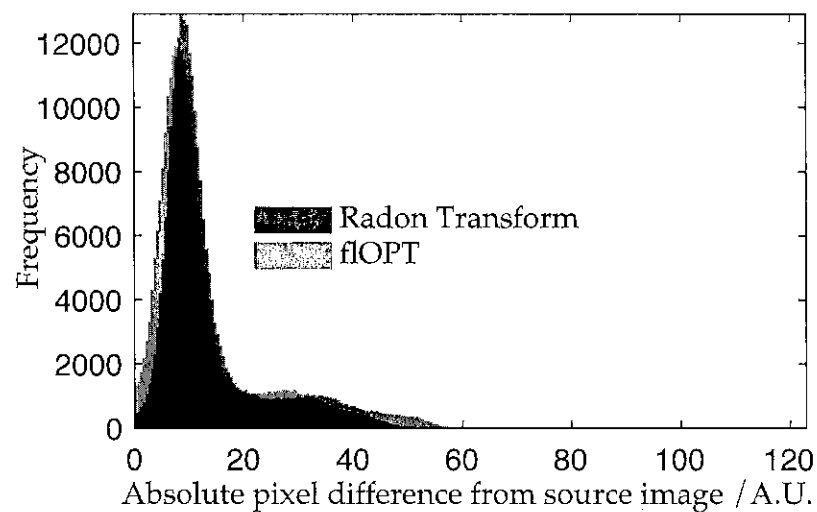
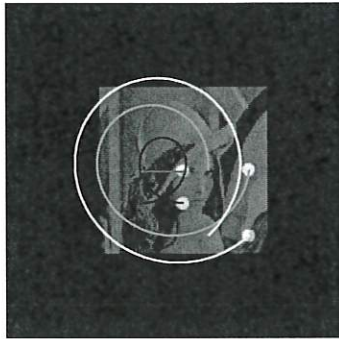
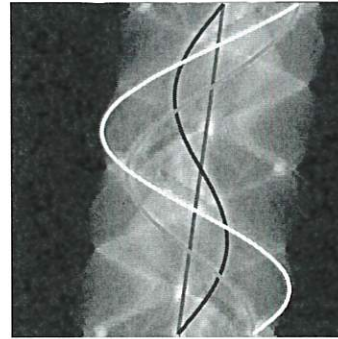


**Fig. 6.10** Histogram of of pixel values compared between reconstructions using fLOPT and the Radon transform. The shift of the histogram to towards overall lower deviance from the source image suggests the fLOPT algorithm out performs the Radon transform

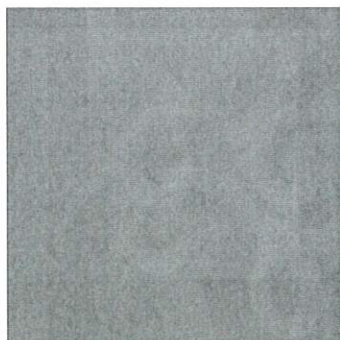


(a) Top down views  $(X, Y)$  of the source image with the fiducial paths marked.  $\curvearrowright (x, x)$



(b) Sinogram  $(v, n)$  of a sample whose axis of rotation has a systematic drift  $\text{---} (v, \theta)$

**Fig. 6.11** Comparison of the two reconstructions under sample imaging with a systematic drift, in 3D though represented here in 2D.



(a) Unfiltered reconstruction using a Radon transform. Axes:  $(X, Y)$



(b) Filtered reconstruction using the new algorithm. Axes:  $(X, Y)$

**Fig. 6.12** Comparison of the two reconstructions under sample imaging with a systematic drift, in 3D though represented here in 2D.



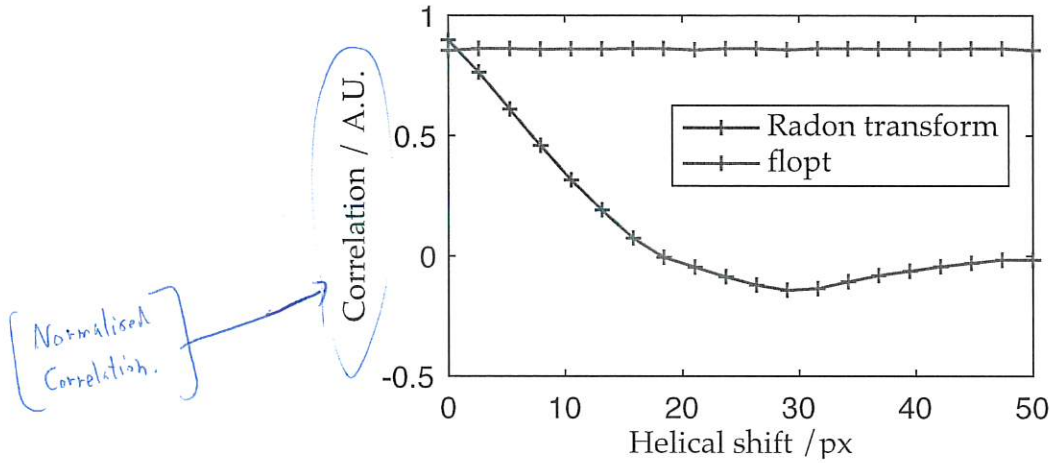


**Fig. 6.13** 2D image correlation of the ground truth and the reconstruction shows that the proposed fLOPT algorithm does not degrade with systematic drift, whereas reconstruction using the standard Radon transform is severely degraded.

#### 6.4.1 Recovery of $\mathbf{R}$ and $\mathbf{T}$ using matrix decomposition

To quantitatively verify that the matrix decomposition technique was valid and robust, the accuracy of the reproduction of  $\mathbf{R}$  and  $\mathbf{T}$  was tested directly. The original  $\mathbf{R}$  and  $\mathbf{T}$  matrices were computed and compared to  $\mathbf{R}$  and  $\mathbf{T}$  generated from matrix decomposition, this absolute difference was computed element-wise in each matrix and then an average for each matrix was taken. Overall the worst case scenario produced a percentage error of 2 % (see Fig. 6.14 for full statistics). The accuracy of the calculated  $\mathbf{R}$  and  $\mathbf{T}$  did deteriorate when adding in additional degrees of combined movement, but with no correlation between the degree of helicity and the error produced. Consistently the translational matrix ( $\mathbf{T}$ ) was more accurately reproduced, this is likely due to there being fewer of degrees of freedom for errors to spread over.

## 6.5 Discussion

A new algorithm for reconstructing OPT data has been demonstrated. The new algorithm uses multiple fiducial markers to recover the matrix which describes the rotation and translation of the sample. The quality of the reconstructions when compared to a standard Radon transform shows a slight improvement, with a great effect when a systematic drift is introduced. The measure the accuracy of the decomposition of  $\mathbf{F}$  into  $\mathbf{R}$  and  $\mathbf{T}$  they were compared to the ground truth matrices.

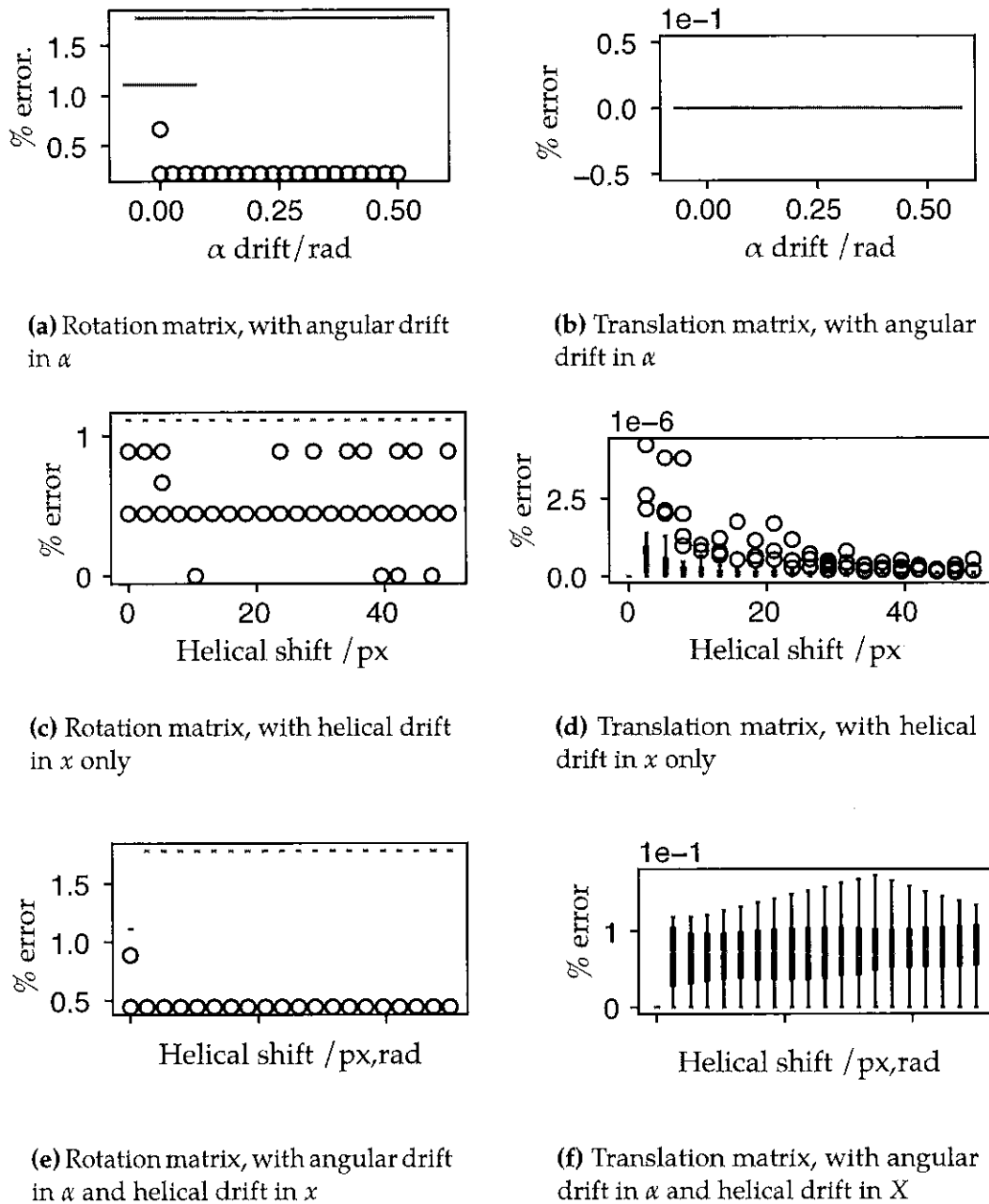


**Fig. 6.14** Box plots demonstrating that the rotational and translations matrices can be recovered accurately from fiducial marker positions. Panels (a) and (b) introduce an angular drift during rotation, to an observer at the detector this would appear as a tip of the sample towards them, causing precession. Panels (c) and (d) introduce a lateral drift in  $X$  causing a helical path to be drawn out. Panels (e) and (f) combine the two effects. In all cases the percentage error introduced by the the addition of undesirable additional movements was on the order of  $<2\%$ .

The element-wise absolute difference  $\left(\frac{|x-y|}{2(x+y)}\right)$  of each matrix was averaged across the matrix for **R** and **T**. In the worst case scenario a maximum of 2 % average absolute difference was found between ground truth and recovered matrices, suggesting the technique is robust to <sup>all</sup> forms of drift and general instability. Such an algorithm could be used to help in minimising ghosting effects seen in real samples; particularly in samples where slipping is likely to occur such as in gels or in cheaper OPT systems which tend to be more mechanically unstable and imprecise.

## 6.6 Future work

### 6.6.1 Bead Tracking

The work presented here is, so far, is a proof-of-concept demonstrated by simulation and reconstruction from ground-truth testcard objectives, and requires several further steps in order apply it to real OPT data. Firstly, a bead-tracking algorithm [65] will need to be created to track multiple beads concurrently in an image series. A sensible approach would be to have a user select the fiducial markers in the image on the first frame and template match in a small window around the selection; this is similar to the algorithm described in Chapter 9. Template matching is robust to occlusions provided the fiducial is not fully eclipsed. If two fiducial markers occlude each other however, this algorithm may switch their identities or both tracking windows may follow one bead. This is a common problem in particle tracking algorithms, but is solved by using a weighted likelihood based on momentum[66].

The likelihood of a bead occlusion occurring will increase with the introduction of additional beads into the sample. As such occluded beads may need to be omitted.

### 6.6.2 Multiple views tracking

The theory backing the proposed algorithm relies on triangulation between two view points. In this work the two view points refer to the image at frames  $n$  and  $n + 1$ . However, it is possible to use three separate views (frames  $n$ ,  $n + 1$  and  $n + 2$ ) to reconstruct a scene, one such approach being quaternion tensors. Working with tensors is computationally and mathematically more challenging, but a future iteration of the algorithm presented here may benefit from using three views to provide a more accurate transformation matrix. Beyond three views there currently

Various

all is too strong, e.g. in case of a piecewise distortion.

reliably

is no mathematical framework at present for four or more views. If such tools did exist, it may be possible to make the algorithm described above as non-iterative and essentially a single shot reconstruction from pixels to voxels.

### 6.6.3 Fiducial free reconstruction

In computer vision scenes often do not contain known fiducial marks and so such marks are found between views. To find such a correspondences, points with similar local texture are found and matched in between each image. This technique is only valid for views with small angles between them, as would be found in OPT. A similar method could be introduced into the algorithm presented here, as each image should have sufficient texture, particularly when using tOPT.

The following chapter will move from improvements in registration using projective matrices and into improves in resolution using on-camera slit-scanning.

Ok!